Biomaterials Science

ROYAL SOCIETY OF CHEMISTRY

PAPER

View Article Online
View Journal

Cite this: DOI: 10.1039/d4bm00949e

Aliphatic polycarbonates with acid degradable ketal side groups as multi-pH-responsive immunodrug nanocarriers†

Adrian V. Hauck,[a] Patric Komforth,[b] Jessica Erlenbusch,[c] Judith Stickdorn,[b] Krzysztof Radacki,[d] Holger Braunschweig,[d] Pol Besenius,[c] Simon Van Herck[e] and Lutz Nuhn *[a]

Pharmacokinetics and biodistribution profiles of active substances are crucial aspects for their safe and successful administration. Since many immunogenic compounds do not meet all requirements for safe and effective administration, well-defined drug nanocarrier systems are necessary with a stimuli-responsive drug-release profile. For this purpose, a novel pH-responsive aliphatic cyclic carbonate is introduced with benzyl ketal side chains and polymerized onto a poly(ethylene glycol) macroinitiator. The resulting block copolymers could be formulated *via* a solvent-evaporation method into well-defined polymeric micelles. The hydrophobic carbonate block was equipped with an acid degradable ketal side group that served as an acid-responsive functional group. Already subtle pH alternations led to micelle disassembly and the release of the active cargo. Furthermore, basic carbonate backbone degradation assured the pH responsiveness of the nanocarriers in both acidic and basic conditions. To investigate the delivery capacity of polymeric micelles, the model small molecule compound CL075, which serves as an immunotherapeutic TLR7/8 agonist, was encapsulated. Incubation studies with human blood plasma revealed the absence of undesirable protein adsorption on the drug-loaded nanoparticles. Furthermore, *in vitro* applications confirmed cell uptake of the nanodrug formulations by macrophages and the induction of payload-mediated immune stimulation. Altogether, these results underline the huge potential of the developed multi-pH-responsive polymeric nanocarrier for immunodrug delivery.

Received 18th July 2024,
Accepted 6th November 2024

DOI: 10.1039/d4bm00949e

rsc.li/biomaterials-science

Introduction

Many promising and highly demanding pharmaceuticals suffer from poor pharmacokinetics, severe side effects and low aqueous solubility.[1,2] Suitable drug-carrier systems can be used to tailor these properties and formulate drug conjugates into promising candidates for medical applications.[3] An intensively investigated platform for such drug-carrier systems is polymeric nanoparticles.[4,5] They can be manufactured in versatile forms, such as polymeric micelles, nanogels, and polymersomes.[6] If composed of biocompatible and biodegradable materials, nanoparticles can improve the transport of active cargos to their target sites, thereby reducing toxicity and premature renal clearance. Commonly used materials for synthetic hydrophilic polymer structures are poly(oxazoline),[7,8] poly(sarcosine),[9] poly(amino acids),[10] and poly(ethylene glycol) (PEG).[11,12] The latter in particular meets several pharmacological requirements, including stealth properties that protect the nanoparticles from protein opsonization, followed by recognition by the innate immune system and blood clearance. Nanoparticle PEGylation increases blood circulation time[13,14] and is therefore often combined with biodegradable hydrophobic polymer materials, including poly(lactides)[15] and poly(carbonates).[16,17] These materials facilitate the encapsulation of water-insoluble drugs but are susceptible to enzymatic hydrolysis within a suitable time frame and thus assure gradual drug release and particle clearance.

With tailored sizes between 10 and 100 nm, synthetic polymeric nanoparticles have been reported to enter tumor tissue

[a]*Chair of Macromolecular Chemistry, Institute of Functional Materials and Biofabrication, Julius-Maximilians-Universität Würzburg, 97070 Würzburg, Germany. E-mail: lutz.nuhn@uni-wuerzburg.de*
[b]*Max Planck Institute for Polymer Research, 55128 Mainz, Germany*
[c]*Department of Chemistry, Johannes-Gutenberg-Universität Mainz, 55122 Mainz, Germany*
[d]*Institute for Sustainable Chemistry and Catalysis with Boron, Julius-Maximilians-Universität Würzburg, 97074 Würzburg, Germany*
[e]*Meinig School of Biomedical Engineering, Cornell University, Ithaca, NY, 14850, USA*

†Electronic supplementary information (ESI) available. CCDC 2371836. For ESI and crystallographic data in CIF or other electronic format see DOI: https://doi.org/10.1039/d4bm00949e

through leaky blood vessels and remain there owing to ineffective lymphatic draining.[6,18,19] This concept, known as the enhanced penetration and retention (EPR) effect, is difficult to translate from *in vivo* models to applications in the human body because of the high variability between individual patients.[20] Nevertheless, a few approved polymeric nanodrug formulations, including DOXIL®, Marqibo® and Genexol®, have demonstrated effectiveness, according to their relevant EPR.[21–23] To further enhance this effect, it is necessary to facilitate nanocarriers with stimulus responsiveness that would allow drug release exclusively at the target site. Environmental changes in the tumor microenvironment, such as an increase in reactive oxygen species (ROS) and redox potential as well as a decrease in oxygen and pH levels, seem to be highly attractive triggers.[24]

Reduced pH gradients are also present upon nanoparticle cell internalization inside endosomes (pH 6.0–5.5) and lysosomes (pH 5.0–4.5).[25,26] Acid-responsive functionalities include hydrazones,[27] orthoesters, oximes,[28] imines,[29] acetals,[30] and ketals,[31] to name a few. Ketals are often used as a linker to modify functional polymer backbones and achieve acid-responsive micelles or nanogels, since they are known to be stable at physiological pH values but degrade within a suitable time window upon acidification.[32–35] The degradation kinetics of ketals can be fine-tuned by regulatory neighboring groups, allowing precise adjustment to the given requirements.[36] Another advantage of a ketal trigger compared to other pH-sensitive triggers is the release of nontoxic small molecules, like acetone, which is listed on the FDA GRAS (generally recognized as safe) list.[37]

Herein, we report the development of an innovative biodegradable nanocarrier based on block copolymers with pH-responsive amphiphilicity. Attached to a gradually hydrolysable aliphatic polycarbonate backbone, acid degradable ketal side groups assure pH-responsive drug formulations that ultimately release their active cargo upon acidification (as found already in the tumor microenvironment or later on during endocytosis, Fig. 1). Besides acid degradability of the micelle-stabilizing side groups, such as gradual hydrolytic carbonate backbone degradation, which is generally accelerated under basic conditions, provides a dual-pH responsiveness in both acidic and basic directions.

To access such carriers, first the synthesis and characterization of a cyclic carbonate monomer bearing an acid degradable ketal side group was demonstrated. Subsequently, this monomer was polymerized under controlled ring-opening polymerization (ROP) conditions into well-defined aliphatic polycarbonates. The acid responsiveness of these polymers was investigated by ^{1}H nuclear magnetic resonance (NMR) diffusion-ordered spectroscopy (DOSY) and size-exclusion chromatography (SEC). Chain extension of the poly(ethylene glycol) yielded amphiphilic block copolymers that could be formulated into narrowly dispersed polymeric micelles. A benzyl moiety stabilizes these micelles *via* π–π-stacking interactions.[38,39] Since this benzyl group is linked to the polymers backbone *via* the ketal functionality, acidification led to rapid micelle disassembly. This degradation process was intensively investigated in a wide range of pH levels by dynamic light scattering (DLS) and UV/vis spectroscopy. Since the polymeric micelles' hydrophobic core allows for the encapsulation of water-insoluble pharmaceutically active ingredients, these micelles can be used as acid-responsive nano-sized drug carriers. The encapsulation of the model compound Nile red revealed selective cargo release exclusively upon micelle degradation, which could be triggered under both acidic as well as basic conditions. Furthermore, drug loading was investigated using the hydrophobic Toll-like-receptor 7/8 agonist CL075. Its stimulus-responsive release in RAW-Blue macrophages demonstrated the polymeric micelles remarkable delivery performance as a multi-pH-responsive biodegradable immunodrug nanocarrier.

Results and discussion

Synthesis of the cyclic carbonate monomer with a ketal-linked benzyl side group (MTC-OE*t*KBn, 14)

For the synthesis of the cyclic carbonate monomer with a ketal-linked benzyl side group (MTC-OEtKBn, **14**), a divergent

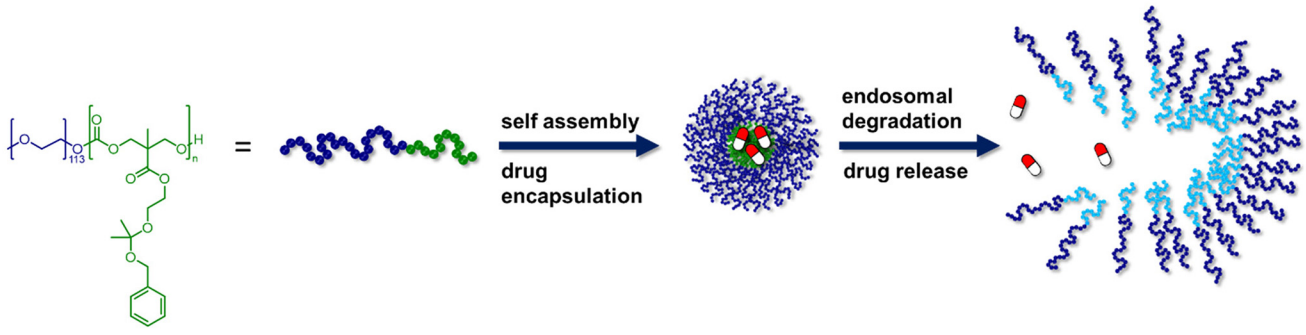

Fig. 1 Amphiphilic block copolymers were synthesized through chain extension of polyethylene glycol ($mPEG_{113}$) with an aliphatic carbonate block. The hydrophobic carbonate block bears acid labile ketal side groups that serve as a pH-responsive trigger. The amphiphilic block copolymers can self-assemble into polymeric micelles that are well-suitable for drug encapsulation. Upon endosomal uptake, the decrease in pH triggers micelle degradation and drug release.

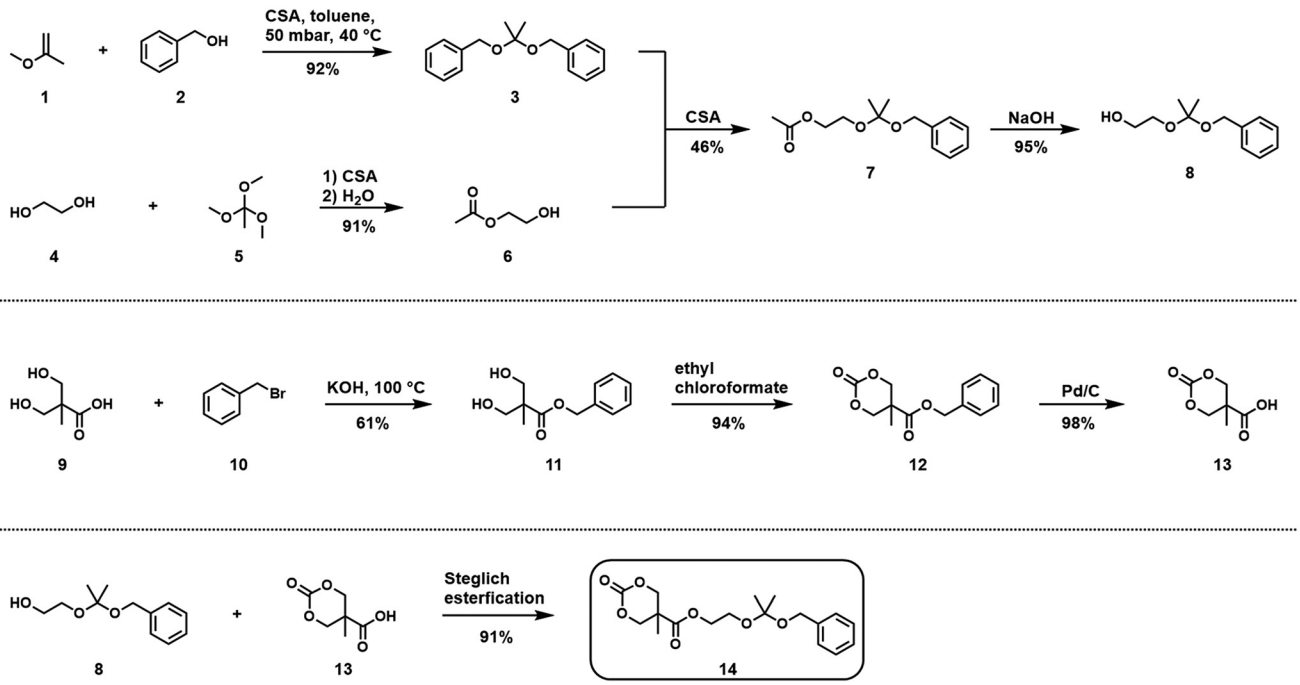

Scheme 1 Divergent synthesis routes for the cyclic carbonate monomer with a ketal-linked benzyl side group (MTC-OEtKBn, **14**). In the upper path, alcohol (**8**) with a ketal-linked benzyl moiety was synthesized. A second synthesis path led to the six-membered cyclic carbonate with a pendant acid group (MTC-OH, **13**). The two intermediates were coupled in a Steglich esterification, yielding MTC-OEtKBn (**14**).

synthesis route was established (Scheme 1). The alcohol (**8**) with a ketal-linked benzyl moiety was synthesized starting from the formation of 2,2-dibenzyloxypropane (BisBnKetal, **3**). In analogy to literature reports,[34] BisBnKetal was obtained by the transacetalization of 2-methoxy propene (**1**) and benzyl alcohol (**2**) catalyzed by camphorsulfonic acid (CSA). Sufficient removal of the formed methanol, which could take part in further transacetalization, was ensured by performing the reaction under reduced pressure. Thereby, the reaction equilibrium was shifted toward the product side, allowing the synthesis of BisBnKetal in very good yields (92%).

In parallel, ethylene glycol (**4**) was asymmetrically protected with trimethyl orthoacetate (**5**) following a standard procedure *via* a cyclic five-membered orthoacetate ring.[40,41] Hydrolysis led to the ethylene glycol monoacetate (EGMA, **6**), again in a good yield (91%). The transacetalization of BisBnKetal (**3**) with EGMA (**6**) yielded the side group component as an acetate-protected alcohol (**7**). Since this type of transacetalization is now a more statistic exchange of benzyl alcohol (**2**) and EGMA (**6**), a product mixture consisting of the two symmetric ketals BisBnKetal (**3**) and Bis(EGMA)Ketal and the desired asymmetric product (**7**) was inevitable. Nonetheless, careful reaction performance allowed accessing yields up to 46%. The basic deprotection of (**7**) afforded the alcohol 2-hydroxyethoxy-2-benzyloxypropane (**8**) almost quantitatively.

In a second synthesis path, 5-methyl-1,3-dioxane-2-oxo-5-carboxylic acid (MTC-OH, **13**) was obtained by a three-step synthesis following a procedure established by Al-Azemi and Hedrick *et al.*[42–44] First, bis-MPA (**9**) was protected with benzyl bromide (**10**) for its acid functionality. Subsequently, the six-membered cyclic carbonate could be formed with ethylene chloroformate. Finally, reductive benzyl ester cleavage *via* Pd/C catalyzed hydrogenation led to MTC-OH (**13**) in an overall yield of 55% (recently, a one-pot synthesis strategy toward MTC-OH (**13**) has been reported without the use of toxic ethylene chloroformate, opening future opportunities for safer syntheses[45]). All the intermediates were characterized by ^{1}H and ^{13}C NMR spectroscopy as well as electron-spray ionization mass spectroscopy thoroughly (ESI-MS, Fig. S1–S21†).

The desired monomer (MTC-OEtKBn, **14**) was finally synthesized by a Steglich esterification of MTC-OH (**13**) and 2-hydroxyethoxy-2-benzyloxypropane (**8**) using *N*,*N*′-diisopropylcarbodiimide (DIC) and 4-dimethylaminopyridine (DMAP). It could be isolated in a good yield (91%) as a colorless crystalline solid. The monomer was successfully characterized by ^{1}H, ^{13}C, and 2D NMR spectroscopy as well as ESI-MS (Fig. S22–S27†). It is worth mentioning that other coupling approaches, *e.g.*, *via* acid chloride chemistry and active pentafluorophenyl ester chemistry, could not yield the desired monomer (**14**). We propose that even under basic conditions the liberated acidic intermediates may still catalyze unfavorable ketal hydrolysis.

Since the ring-opening polymerization of cyclic carbonates is highly prone to side reactions, the purity of all the reactants is essential. Thus, the monomer was carefully purified by column chromatography and subsequent recrystallization from diethyl ether. The collected material was finally characterized by crystal structure determination, with the results pro-

vided in Fig. S28 and Table S1.† The twisted ring confirmation suggested a preferable reactivity toward ring-opening polymerization (ROP).

Synthesis of PB-p(MTC-OEtKBn)$_n$ homopolymer *via* ring-opening polymerization (ROP) of MTC-OEtKBn (14) and investigation of its pH responsiveness

To demonstrate the polymerizability of MTC-OEtKBn (**14**) and to investigate the acid degradability of the reactive side groups along the polymer chain, a homopolymer was first synthesized (Fig. 2A). Pyrene butanol (PB, **15**) was used as an initiator (M : I = 20 : 1) under base-catalyzed ring-opening polymerization (ROP) conditions. To exclude side reactions, it was necessary to use highly pure reactants. Thus, both educts were dried by azeotropic distillation with benzene. The reaction was conducted in DCM and catalyzed by 1,8-diazabicyclo[5.4.0]undec-7-ene (DBU), with both dried over calcium hydride prior to use. To achieve better control in the polymerization, the reaction was carried out under an inert gas atmosphere (N_2) at −20 °C. It was aimed to quench the polymerization at a monomer conversion of 70%–80% to avoid an increase in the dispersity. For monitoring the reaction progress, samples were withdrawn from the reaction mixture at intervals of 30 min and subsequently analyzed by ^{1}H NMR spectroscopy (Fig. S29†). The kinetic plot of the logarithmic reciprocal monomer conversion p *versus* the reaction time t showed a linear trend (Fig. 2B), underlining the controlled living nature of the chain-end polymerization following linear first-order kinetics. After 3.5 h the reaction was quenched at a monomer conversion of 73%. Thereby, a narrowly distributed homopolymer (**16**) was obtained, which was successfully characterized by ^{1}H and ^{13}C NMR spectroscopy, gel permeation chromatography (GPC), and MALDI-TOF mass spectrometry (Fig. 2C, D and Fig. S30–35†). The ^{1}H NMR spectrum showed characteristic broadened signals that could be assigned to the expected polymer structure (Fig. S30 and 31†). Referencing the polymer signals to the pyrene butanol signals provided a degree of polymerization (DP) of 13.4, which was only slightly lower than the theoretical DP of 14.6 (at a conversion of 73% and a monomer to initiator ratio of M : I = 20 : 1). The structure was

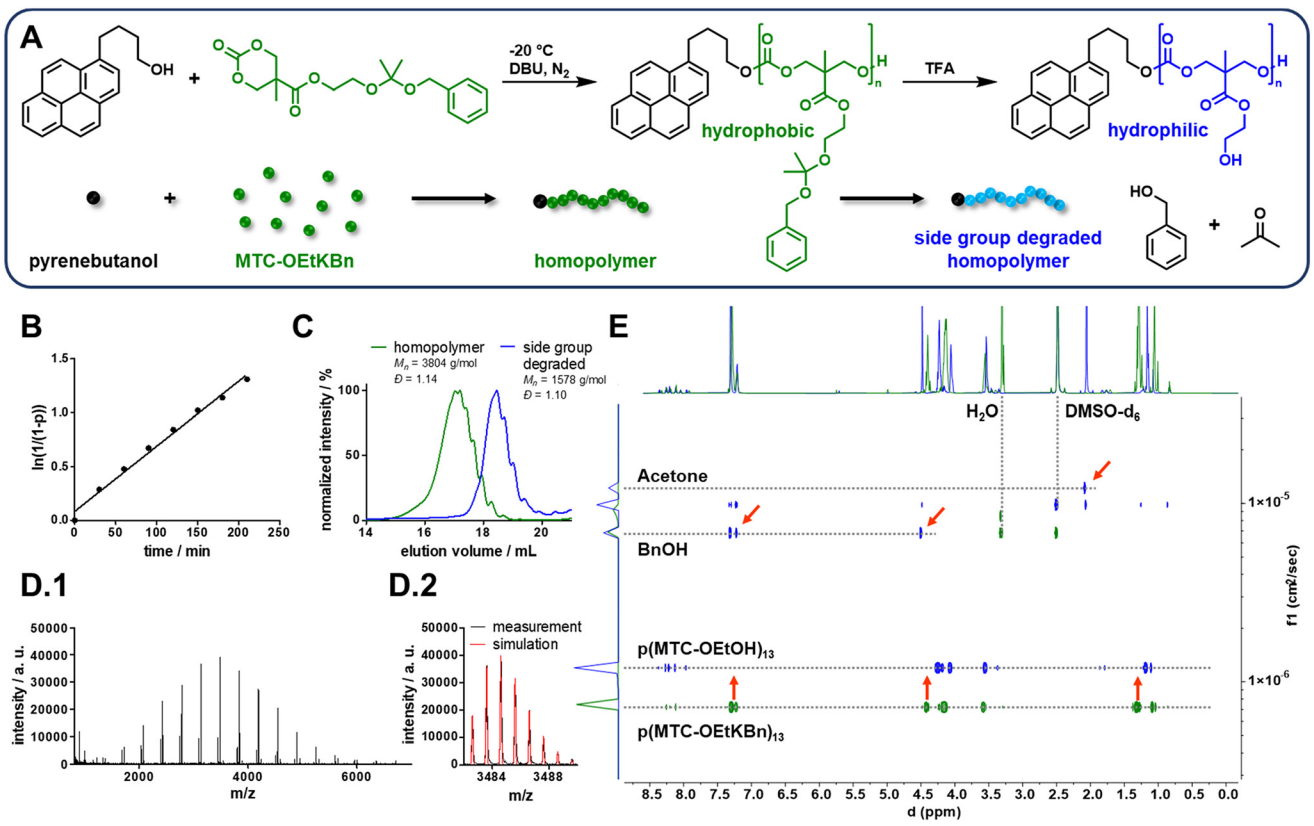

Fig. 2 Homopolymerization of MTC-OEtKBn (**14**). A: Synthesis scheme of ring-opening polymerization (ROP) using 1-pyrenebutanol as the initiator and DBU as the catalyst (M : I : C = 20 : 1 : 1) in DCM under a nitrogen atmosphere. Acidification with trifluoroacetic acid (TFA) led to side group hydrolysis and transformation of the hydrophobic polycarbonate into a hydrophilic one. B: Kinetic plot revealing the controlled living nature of the chain-end polymerization for MTC-OEtKBn homopolymerization. C: Gel permeation chromatography (GPC) elugram of the homopolymer (green) and side-group-degraded homopolymer (blue). D.1: Matrix-assisted laser desorption ionization time of flight (MALDI-TOF) mass spectrum of the homopolymer and D.2 section of a single isotope pattern and simulation of one peak (corrected by +0.13 m/z). E: Diffusion-ordered ^{1}H NMR spectra (DOSY) of the homopolymer (green) and side-group-degraded homopolymer (blue); red arrows mark the benzyl alcohol and acetone signals, shifted toward smaller diffusion coefficients, after hydrolysis.

further confirmed by ^{13}C NMR spectroscopy, showing *e.g.* a characteristic dimethylketal carbon signal at 99.85 ppm (Fig. S32†), which confirmed that the applied polymerization conditions did not affect the pH-labile side group. Further, diffusion-ordered ^{1}H NMR spectroscopy measurements revealed the presence of one single polymer species with a distinct macromolecular diffusion coefficient (Fig. 2E and Fig. S33†). The GPC elugram recorded by UV absorbance confirmed the narrowly distributed polymer ($Đ$ = 1.14, Fig. 2C, green line – note that individual oligomers could even be resolved in the RI-recorded elugram at lower molecular weights, and at high molecular weights, a minor shoulder could be found, indicating the formation of the homopolymer by self-initiation, thus lacking the UV-sensitive pyrene group, Fig. S34†). Moreover, MALDI-TOF mass spectrometry confirmed the presence of a narrow polymer distribution (Fig. 2D.1 and Fig. S35†). Additionally, the isotope patterns of the single peaks matched with the theoretical simulation, providing further evidence for the successful synthesis of the desired homopolymer (Fig. 2D.2).

Finally, successful ketal hydrolysis in an acidic environment was evidenced by diffusion-ordered ^{1}H NMR spectroscopy (DOSY) and GPC. The addition of trifluoroacetic acid (TFA) to the NMR sample led to the formation of a new polymer species with a smaller diffusion coefficient, whose ^{1}H NMR signals showed the absence of ketal and benzyl alcohol units (red arrows in Fig. 2E and Fig. S36†). Besides, the formation of the small molecule fragments benzyl alcohol and acetone could be observed, underlining the ability of the homopolymer to meet the desired acid responsiveness. The GPC of this side-group-degraded polymer revealed a shift toward smaller molecular weight species compared to the original homopolymer, as expected (Fig. 2C, blue line, Fig. S37†), indicating acid-triggered side chain fragmentation, too.

Synthesis of mPEG$_{113}$-*b*-p(MTC-OEtKBn)$_n$ block copolymers

Substituting the 1-pyrenebutanol initiator by a 5 kDa poly (ethylene glycol) macro initiator (mPEG$_{113}$-OH, **17**) allowed the synthesis of amphiphilic block copolymers for the later formulation of polymeric micelles (Fig. 3A). A monomer/macroinitiator ratio of 30 : 1 was chosen to achieve a sufficiently large carbonate block. The purity of the reactants and the absence of traces of water were again ensured by azeotropic distillation with benzene and the drying of DCM and DBU over calcium hydride. In analogy to the homopolymerization, the synthesis of block copolymers was also well-controlled under the applied reaction conditions and followed controlled living chain-end polymerization conditions (a linear trend could be derived in the kinetic plot of the logarithmic reciprocal monomer conversion *p versus* the reaction time *t*, Fig. 3B). At a monomer conversion of 89%, the polymerization was quenched by precipitation of the reaction mixture in ice-cold *n*-hexane. A waxy white solid was collected and characterized. The GPC elugram revealed a wide mass distribution that was assumed to be a

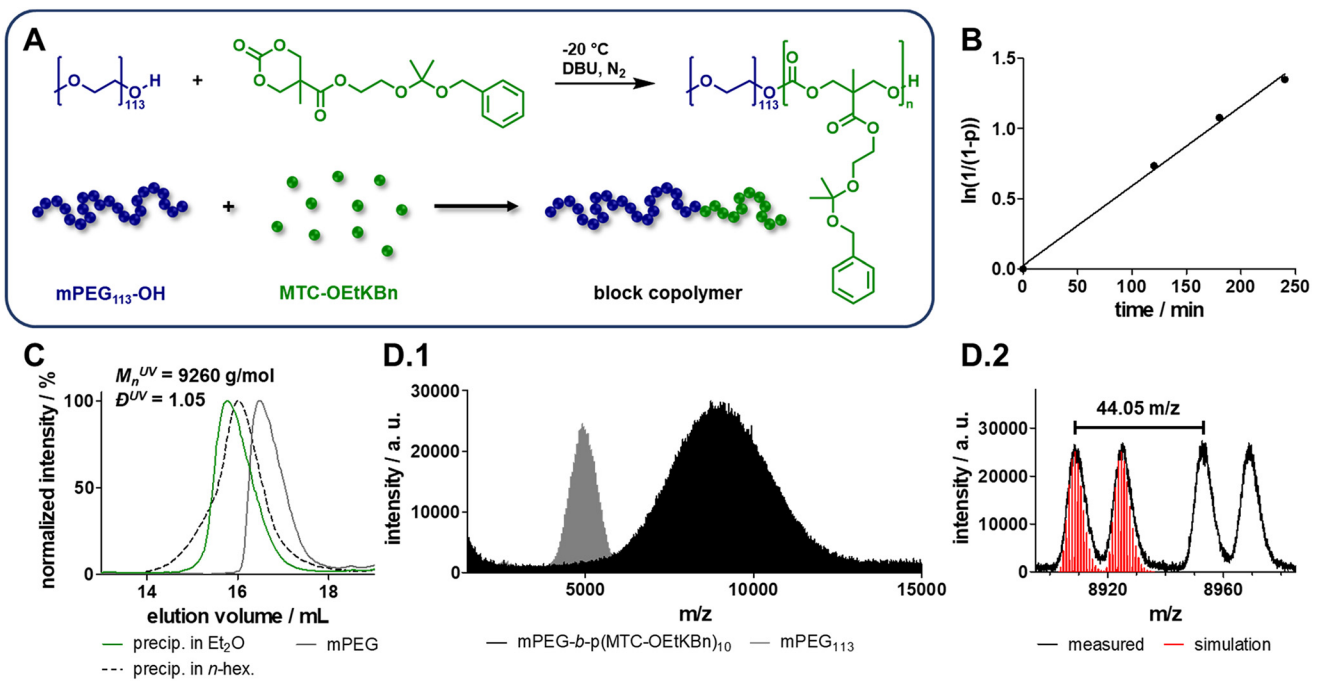

Fig. 3 Block copolymer synthesis. A: Synthesis scheme of the ring-opening polymerization of MTC-OEtKBn (**14**) using mPEG$_{113}$-OH (**17**) as the macroinitiator and DBU as the catalyst (M : I : C = 30 : 1 : 1) in DCM under a nitrogen atmosphere. B: Kinetic plot, revealing the living nature of block copolymer synthesis. C: Section of the polymer's GPC elugram after precipitation in *n*-hexane (dashed line) and after precipitation in diethyl ether (green) next to the GPC elugram of the mPEG$_{113}$-OH macro initiator (gray). D.1: Matrix-assisted laser desorption ionization time of flight (MALDI-TOF) mass spectrum of the block copolymer (black) next to the mass spectrum of the mPEG$_{113}$-OH macroinitiator (gray) and D.2 section of two species with distinctive block lengths and simulation (±0 *m*/*z*) of mPEG$_{113}$-*b*-p(MTC-OEtKBn)$_{11}$ cationized with Na^+ and K^+, respectively.

result of the anticipated block copolymer formation; however, also minor simultaneous homopolymer formation took place by self-initiation of the monomer as a side reaction (dashed line in Fig. 3C and Fig. S39†).

Fortunately, redissolving the polymer and precipitating it in ice-cold diethyl ether allowed for the removal of the undesired homopolymer (up to 40%) from the targeted block copolymer. The latter could be isolated as a white amorphous powder (**18**) at yields of at least 60%. A narrow mass distribution ($Đ$ = 1.05) without any shoulder was now obtained by GPC (green line in Fig. 3C and Fig. S39†). MALDI-TOF mass spectrometry provided a narrow signal of significantly higher molecular weights than the $mPEG_{113}$-OH initiator, too (Fig. 3D.1 and Fig. S40†). The MALDI-TOF mass spectra allowed for assigning each of the single peaks to a specific block copolymer species with distinctive repeating units (Fig. 3D.2). Characterization of the block copolymer by ^{1}H NMR spectroscopy further confirmed the successful synthesis (Fig. S38†). The NMR-derived number of repeating units was 10, which was on the one hand significantly smaller than the expected value of 26.7 (this value was consistent with the observed monomer consumption due to homopolymer formation), but on the other hand, the straightforward purification process and the acceptable yields of pure the block copolymer can facilitate the application of this highly functional and multi-pH-responsive material in further block copolymer self-assembly studies.

Self-assembly of $mPEG_{113}$-*b*-p(MTC-OEtKBn)$_n$ into polymeric micelles and acidic degradation study

To demonstrate the suitability of the synthesized amphiphilic block copolymers as nanocarriers, their capability to self-assemble into polymeric micelles was investigated. For this purpose, a solvent-evaporation method described by Bagheri *et al.*[46] and Czysch *et al.*[17] was applied to the hydrolytically degradable block copolymers. During this process, the block copolymers (and if required the water-insoluble cargo for encapsulation) were dissolved in acetone. The mixture was then added to DI water (or buffer) in a vial and the open vial was stored in a sterile lamina flow hood overnight, allowing the acetone to evaporate. The slow transition of the good solvent into a poor solvent (with respect to the polycarbonate block) led to a controlled self-assembly of the block copolymers into well-defined polymeric micelles (Fig. 4A).

The formulated nanoparticles were analyzed by dynamic light scattering (DLS) and a narrow nanoparticle size distribution with a diameter of 35.7 nm and a PDI of 0.17 were found (Fig. S41†). Further analysis of the polymeric micelles by transmission electron microscopy (TEM) confirmed the formulation of spherical nanoparticles at similar small sizes and narrow distributions, too (Fig. 4B and Fig. S42A.1–4†). The diameters of 100 randomly chosen spherical particles were measured by the software ImageJ and an average particle diameter of 29 ± 4 nm was obtained (Fig. S42B and C†). Compared to the DLS results, the particles appeared slightly smaller, which may be due to the fact that the solvent was removed during the TEM sample preparation. Another reason could be a poor contrast with the micelles' PEG corona. Nonetheless, both methods led to similar sizes and were therefore in good agreement.

To get a deeper understanding of which concentrations these polymeric micelles are stable at, the critical micelle concentration (CMC) was determined. For this purpose, pyrene-loaded polymeric micelles were formulated. Depending on the polarity of the pyrene environment, a change in the I_3 fluorescence band can be detected, which can be used to evaluate whether pyrene is encapsulated in the hydrophobic core of a polymeric micelle or if it is exposed to the hydrophilic solvent. Making use of these properties, a dilution series of pyrene-loaded polymeric micelles was investigated, finally giving a CMC of 131 nmol L^{-1} (Fig. S43†). This low CMC allows for applications even in very diluted conditions, as particularly relevant in *in vitro* and *in vivo* studies.

After successful polymeric micelle formulation, the nanoparticles' degradation upon acidification was investigated. While intact side groups stabilized the polymeric micelles through hydrophobic and π–π-stacking interactions, ketal hydrolysis led to the loss of these adhesive forces accompanied by a transition of the hydrophobic polycarbonate block into a hydrophilic one (Fig. 4C). The loss of amphiphilicity further supported the polymeric micelles' disassembly due to swelling of the micelles core, pushing the single polymer chains further apart. This degradation process was intensively investigated by DLS. For this purpose, polymeric micelles were incubated in different buffered solutions (PBS or acetate buffer) within a pH range of 3.6–7.4. For that purpose, a concentrated micelle stock solution (β = 10.0 mg mL^{-1}) was first prepared in DI water *via* the solvent-evaporation method. Then, aliquots of this stock solution were diluted 10 : 1 (v/v) into the different buffers. Immediately after mixing, DLS measurements were repeatedly conducted over a period of 56 d. The derived count rates were used as an indication of micellar integrity (Fig. 4D.1). As expected, the polymeric micelles degraded rapidly at low pH values and became gradually more stable under milder conditions. The decline in the normalized derived count rate could be fitted by a one-phase exponential decay function, indicating first-order ketal hydrolysis. From this decay function, the micelles half-life times at different pH values were calculated. The endosomal pH value of 5.5 could be realized by PBS as well as acetate buffer. Both conditions showed the same decay underlining the comparability of the two buffered systems (of note, the PBS sample at pH 5.5 provided some aggregates after 7 d, probably because of salt precipitation formation, and therefore it was not considered anymore after this time point). The micelles' half-life at this pH value was 2.80 d (PBS) and 2.58 d (acetate buffer), respectively (Table S2†), which were within the desirable range for cargo release.[47] For higher pH values, longer delayed degradations were recorded, even at pH 7.0 a decrease in the derived count rate could be observed, however only starting after ~300 h. This was again still consistent with all the other measurements (of note, at pH 7.4 a minimal increase in count rate was observed that was presumably caused by insufficient

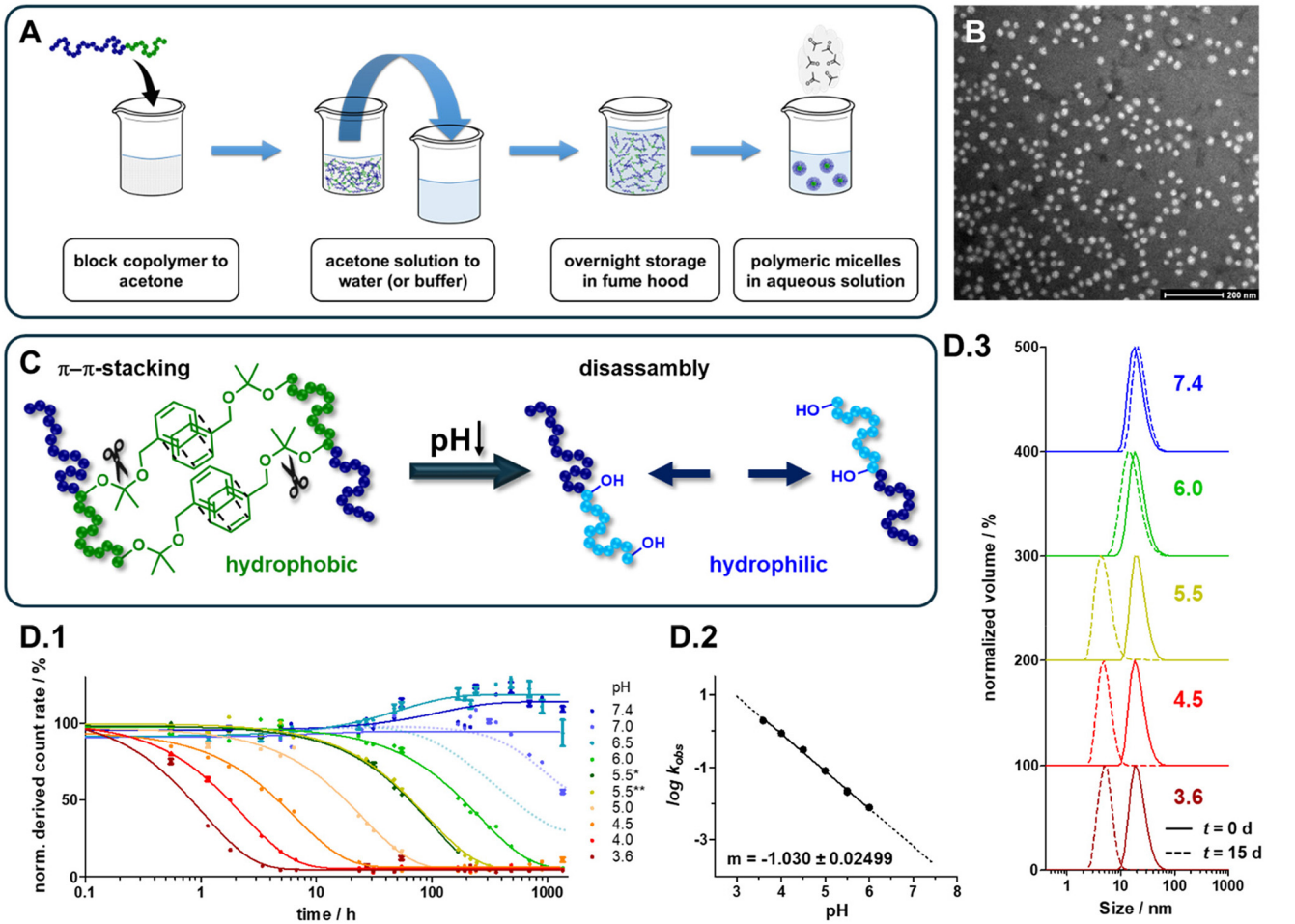

Fig. 4 A: Schematic polymeric micelle formulation using the solvent-evaporation method. The block copolymer was dissolved in acetone and the solution was added to water (or a buffer). The homogeneous mixture was left uncapped and stored in a fume hood overnight. Acetone evaporation led to the slow transfer from a good solvent to a bad solvent (with respect to the hydrophobic polycarbonate block) initiating polymeric micelle self-assembly. B: Transmission electron spectroscopy (TEM) image of spherical polymeric micelles. C: Schematic ketal side group hydrolysis upon acidification; the loss of π–π-stacking interaction forces and the loss of amphiphilicity led to micelle degradation. D.1: Polymeric micelle degradation study performed by dynamic light scattering; the normalized derived count rate declined within different time frames, depending on the pH value, indicating micelle disassembly. D.2: Log $k_{obs.}$–pH-plot of the degrading polymeric micelles. D.3: Polymeric micelles size distribution at t = 0 (solid line) and after 15 d (dashed line) for different pH values.

sealing of the DLS cuvette leading to water evaporation – this was also the case at pH 6.5; however, a decrease appeared after ~300 h because of the expected particle degradation). Altogether, the trends for the micelle degradation at pH 3.6–6.0 (as well as the anticipated behaviors at pH 6.5 and 7.0, sketched with dashed lines) are summarized in Fig. 4D.1. In conclusion, under physiologic conditions (pH 7.4) the polymeric micelles remained stable over the whole observation period; while upon gradual acidification, accelerated micelle disassembly could be observed. These findings can be further underlined by the changes in the size distributions comparing at t = 0 d and t = 15 d (Fig. 4D.3). While no change was observed at pH 7.4, a slight shift toward smaller diameters could be seen at pH 6.0. Under endosomal (pH 5.5), lysosomal (pH 4.5), and strongly acidic conditions (pH 3.6), the polymeric micelles were entirely disassembled.

The logarithm to the base 10 (log) of the observed degradation rate constant $k_{obs.}$ was plotted against the pH value (Fig. 4D.2). The observed rate constant $k_{obs.}$ was actually composed of a linear combination of the first-order rate constant for non-catalyzed degradation in water only k_0 and the second-order rate constants for its degradation catalyzed by protons k_H, as described in eqn (1).[48,49]

$$k_{obs.} = k_0 + k_H[H^+] \quad (1)$$

Since the slope of the log($k_{obs.}$)–pH-profile corresponds to k_H and approached the value −1 (m = −1.03 ± 0.02), this indicates that the observed ketal hydrolysis followed a specific single-proton-catalyzed hydrolysis mechanism. Only one single proton was involved in the hydrolysis mechanistically, which finally resulted in the acid-triggered disassembly of the block

copolymer micelles. Assuming a continuous linear trend of this log($k_{obs.}$)–pH-profile, the polymeric micelles half-life under physiologic conditions (pH 7.4) could be estimated to be 220 d (not taking into account the water-mediated carbonate backbone decay, as observed for aliphatic polycarbonate nanocarriers earlier).[12,16] These findings underline the appealing properties of the nanoparticles as a physiologically stable carrier system that only release their cargo upon a drop in the pH, which is conceivable during endocytosis or accumulation in acidified tumor tissues.

Nile red release study and *in vitro* internalization of dye-loaded polymeric micelles by RAW-Blue™ macrophages

To investigate cargo release from the carrier system, the water-insoluble model compound Nile red was chosen and encapsulated into polymeric micelles by the solvent-evaporation method. Nile red is particularly suitable for release studies in aqueous environments, since it has a strong absorption at 547 nm while being located in a hydrophobic milieu (present in the micellar core) but barely absorbs light in aqueous environments (after release).[50,51]

Nile red (2.5 wt%) was added to a concentrated polymer solution (β = 10.0 mg mL^{-1}) in acetone. This solution was mixed with DI water and stored in the fume hood overnight. After complete acetone evaporation, the finished formulation was diluted in different buffers. Alongside physiological (pH 7.4) and endosomal (pH 5.5) model-environments, also a basic (pH 9.5) buffer was chosen. The latter served to investigate the aliphatic carbonate block backbone hydrolysis under base-catalyzed conditions (which was also likely to be enzymatically mediated, as reported for bulk materials at neutral pH[52,53]). Compared to the acidic degradation, where the ketal side group was hydrolyzed and a hydrophilic block copolymer remained, the base-catalyzed carbonate hydrolysis led to a complete backbone degradation and the formation of mPEG$_{113}$-OH and small molecule fragments (Fig. 5A). Under physiological conditions (PBS), the micelles could be expected to be stable.

The three samples were simultaneously analyzed by DLS and UV/vis spectroscopy. The DLS-detected derived count rate provided an insight into the polymeric micelles' integrity, while the UV/vis spectra allowed for quantification of Nile red release from the micellar core. According to the derived count rate, the polymeric micelles remained stable at physiologic pH 7.4 but degraded in acidic (pH 5.5) and basic (pH 9.5) environments (Fig. 5C). This decay was accompanied by a simultaneous decline in the Nile red absorption detected by UV/vis spectroscopy (Fig. 5B.1–4). Interestingly, both observations were very much synchronized and suggested cargo release as an exclusive result of polymeric micelle degradation. Consequently, theses polymeric micelles are considered to enable long-time stable cargo encapsulation as well as targeted release only at anticipated variations of the pH conditions.

Encouraged by these results, *in vitro* studies were performed to demonstrate the internalization of the polymeric micelles by RAW-Blue™ macrophages. For this purpose, Rhodamine B octadecyl ester-loaded polymeric micelles (β = 1.0 mg mL^{-1}) were formulated under sterile conditions (0.33 wt% dye loading, 13.2% encapsulation efficiency, Fig. S44†). Confocal fluorescence microscopy imaging revealed a distinct polymeric micelle uptake by the macrophages (Fig. 5D), which was in strong contrast to the PBS control group. Furthermore, flow cytometry (FC) experiments showed a pronounced shift of the mean fluorescence intensity, demonstrating effective micelle uptake by all the considered macrophages (Fig. 5E and Fig. S45†).

Plasma stability of immunodrug-loaded polymeric micelles and *in vitro* drug administration

To ensure the PEG provides a stealth effect, it is important that proteins from the blood plasma do not adsorb or aggregate with the nanodrug formulation. Otherwise, recognition and clearance by the innate immune system can prevent long-time circulation (Fig. 6A).

For this purpose, light-scattering studies can be conducted in human blood plasma and evaluated according to Rausch *et al.*[54] in order to estimate probable interactions between nanoparticles and the blood plasma components. Using the solvent-evaporation method, the TLR7/8 agonist CL075 was again encapsulated in polymeric micelles, aiming for a drug loading of 5.0 wt%. Their nanoparticles sizes were then first determined by conventional DLS (Fig. S46A†) as well as multi-angle DLS measurements (Fig. S46B†), affording similar results. The latter technique was then applied to determine the scattering autocorrelation curves of full human blood plasma alone and incubated with the particles (Fig. S46C†). According to Rausch *et al.*,[54] the autocorrelation curves of nanoparticles in human blood plasma can be evaluated by the linear combination of the determined individual autocorrelation curves of the particles and blood plasma as long as no interaction/aggregation occurs. Fortunately, the CL075-loaded polymeric micelles could nicely be fitted by the two predetermined autocorrelation curves at several scattering angles, which was therefore indicative of there being no protein aggregation (Fig. 6B and Fig. S46C†). Consequently, for controlled systemic applications, the pH-sensitive drug-loaded polymeric micelles could remain stable even under complex biological conditions and, thus, provide ideal features for further applications.

In this respect, *in vitro* studies were finally performed to evaluate the payload's biological activity. For the Toll-like receptor (TLR) 7/8 agonist CL075, we applied the particles on a RAW-Blue™ macrophage reporter assay. Upon addressing the cells' TLR and initiating their intracellular NFκB pathway, the cells secrete an alkaline phosphatase into the cell culture medium, whose activity can be determined by the Quanti-Blue™ assay. Afterwards, the cells can further be evaluated by MTT assay for their viability after exposure to micellar particles, too. For this purpose, drug-loaded polymeric micelles were again formulated under sterile conditions, with a targeted CL075 loading of 2.0 wt%. As references, empty micelles and a formulation of free drug were prepared in analogy (note that

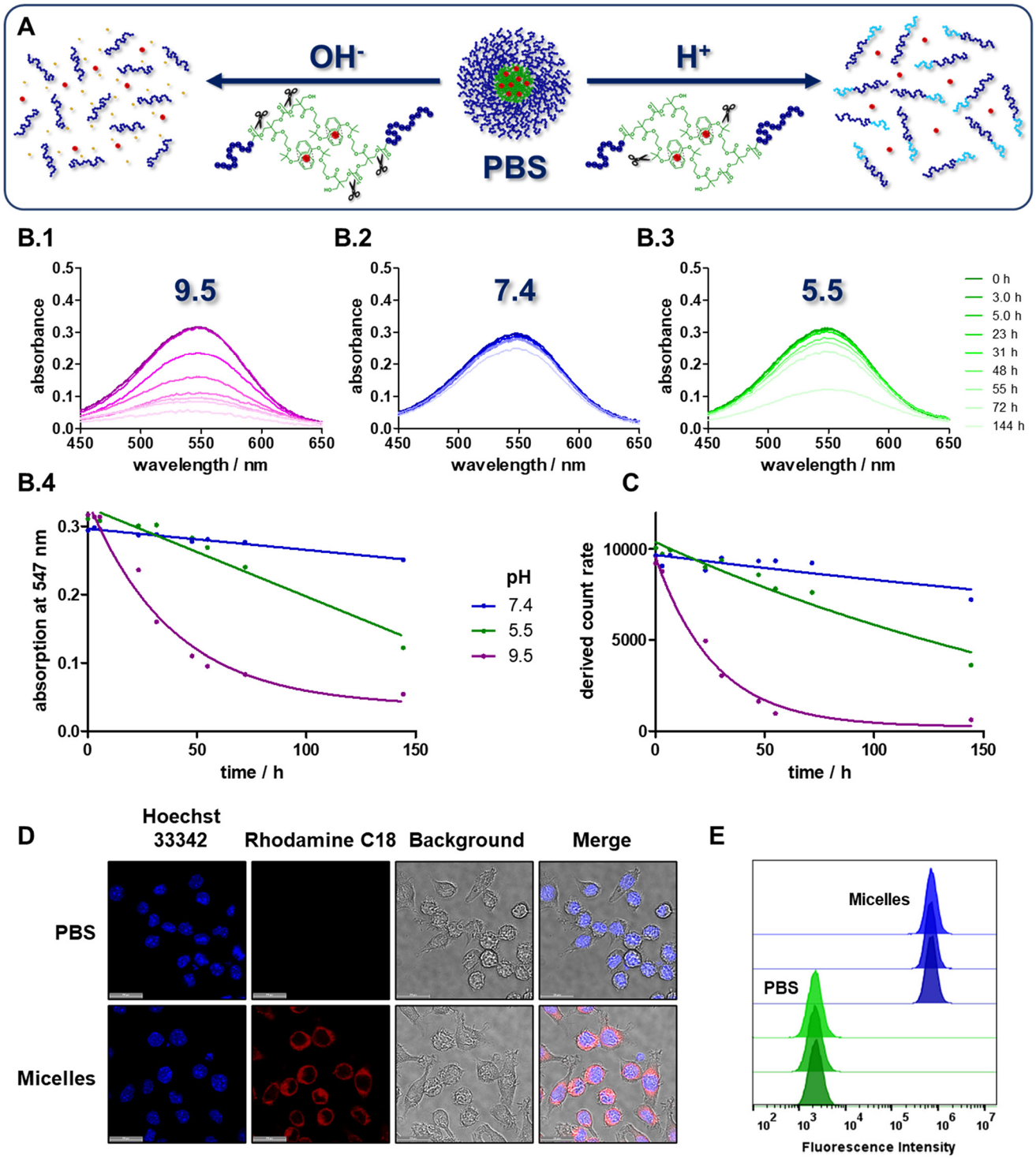

Fig. 5 A: Schematic polymeric micelle degradation in acidic and basic environments. A low pH value led to side group ketal hydrolysis, which induced micelle degradation as a result of the loss of π–π-stacking interactions and amphiphilicity. A high pH value on the other hand led to carbonate backbone hydrolysis and the formation of single-chain $mPEG_{113}$-OH homopolymers and small molecule fragments. In contrast, the polymeric micelles were stable at physiologic conditions. B: UV/vis absorption spectra of encapsulated Nile red over a period of 144 h at pH 9.5 (B.1), pH 7.4 (B.2), and pH 5.5 (B.3). B.4: Time-dependent decline of the UV/vis absorption maxima owing to Nile red release. C: Decline of the derived count rate, detected by DLS as an indication of the polymeric micelle degradation. D: Confocal fluorescence microscopy pictures of RAW-Blue™ macrophages incubated with PBS or Rhodamine B octadecyl ester-loaded polymeric micelles (red); nuclei stained with DAPI (blue). E: Flow cytometry histogram showing the cellular uptake of Rhodamine B octadecyl ester-loaded polymeric micelles by RAW-Blue™ macrophages (n = 3, blue) in comparison to Raw-Blue™ macrophages incubated with PBS (n = 3, green).

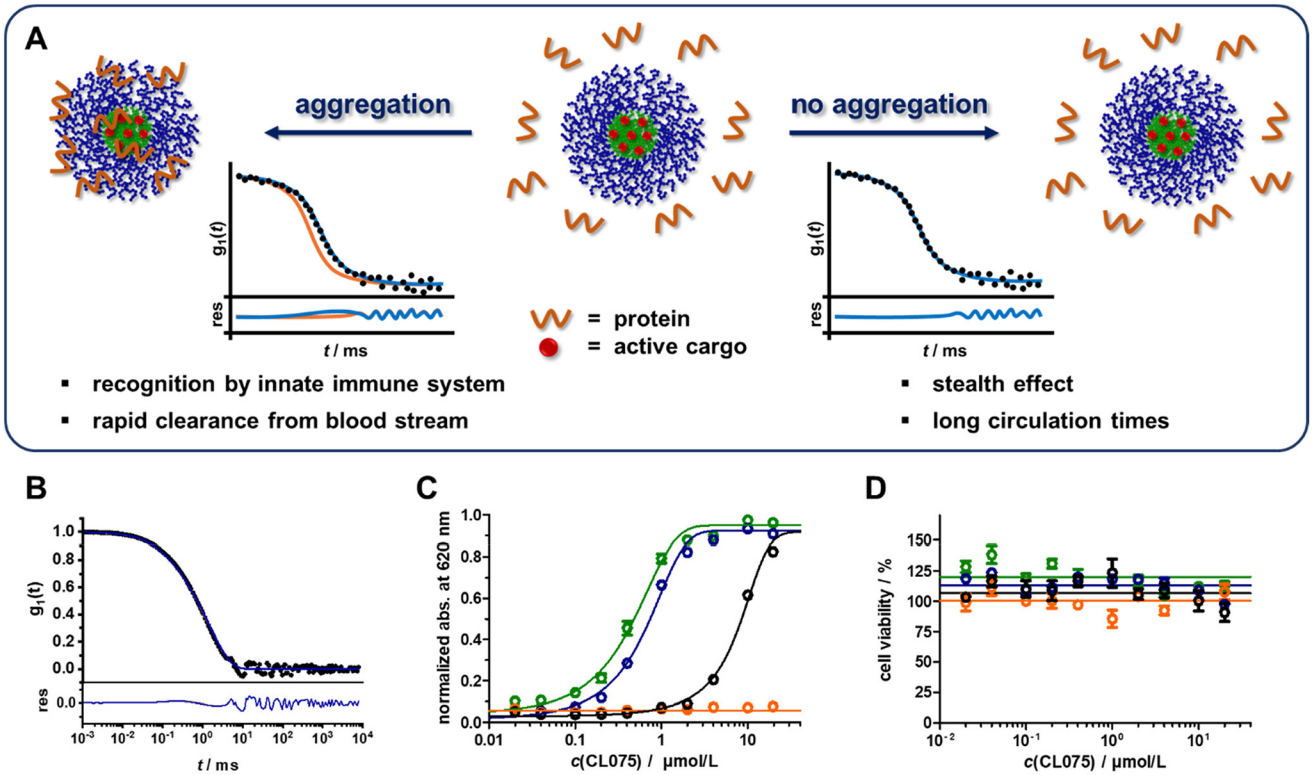

Fig. 6 A: Schematic protein interactions of polymeric micelles: in human blood plasma, when the nanoparticles encapsulating a hydrophobic payload interacted with proteins and formed aggregates, the obtained multi-angle DLS autocorrelation curves could not be fitted by the sum of the individually determined autocorrelation curves of the particles and blood plasma alone (left). This could only be achieved when the particles remained stable and did not interact with the plasma proteins (right). B: Results of the multi-angle DLS analysis of CL075-loaded polymeric micelles in human blood plasma. Shown are the autocorrelation curves, measured at an angle of 70°, for the micelles loaded with 5.0 wt% CL075. The autocorrelation curves were recorded after 1 h incubation in human blood plasma and compared to the sum of the autocorrelation curves obtained from individual measurements of the plasma and micelles. C: QUANTI-Blue™ assay of the cell culture supernatant to determine the TLR7/8 stimulation (n = 4). D: MTT assay results of the remaining cells, demonstrating the unaffected cell viability for all the samples (n = 4).

the drug alone was not soluble in PBS and precipitated out during the formulation process – compare Fig. S47A†). The nanoparticles were characterized by DLS, and the drug loading was determined by UV/vis spectroscopy (1.94 wt% drug loading, 97.2% encapsulation efficiency – Fig. S47†). A dilution series of all the samples was prepared in a CL075 concentration range of 0.02–20 µmol L^{-1}. For a better insight, the assays were also performed with a positive control of CL075 prepared from a 25 mg mL^{-1} DMSO stock solution diluted into cell culture medium. As shown in Fig. 6C, the micelle-guided CL075 transport stimulated the TLR 7/8 at a similar dose range as the positive CL075 reference. The CL075 formulation in the absence of a carrier on the other hand revealed a decreased immune stimulation by one order of magnitude, while the empty nanocarrier did not activate the NFκB pathway within the investigated concentration window but remained immunosilent (Fig. 6C). These findings underline the necessity of a nanocarrier for the solubilization of hydrophobic drugs and point out the suitability of the elaborated polymeric micelles to serve such a purpose. Thereby, the drugs' receptor activity was also fully retained.

Besides, the MTT cell viability assay successfully demonstrated the absence of any cellular toxicity for all the investigated formulations in the applied concentration regime. In addition, the cytotoxicity of the side-group-degraded polymers was investigated to exclude any toxicity, even after the delivery process (Fig. S48†). For this purpose, polymeric micelles were formulated in PBS and half of the sample was treated with 10 vol% of 1 M hydrochloric acid (Fig. S48A†). After confirming full degradation by DLS (Fig. S48B†), the former pH value was restored by adding the same amount of 1 M sodium hydroxide. Both samples did not show any cytotoxicity within the tested concentration range (which was equal to the carrier concentration range used in the assays before, Fig. S48C.1†). Furthermore, the cytotoxicity of the degradation products acetone and benzyl alcohol as well as a combination of both was investigated, too. Again, no reduced cell viability could be found (Fig. S48C.2†). Altogether, these findings suggest the pH-responsive polycarbonate block copolymer micelles with hydrophobic benzyl ketal moieties could serve as effective immunodrug nanocarriers with intriguing degradation profiles.

Conclusion

In this study, the design and synthesis of a novel acid-responsive cyclic carbonate monomer pave the way for a new versatile platform of biocompatible nanocarriers. The elaboration of a robust synthesis route and characterization of all the intermediates yielded the final monomer, which was susceptible to base-catalyzed ring-opening polymerization under controlled living chain-end polymerization conditions. A homopolymer was prepared from this monomer and provided narrow molecular weight distributions. Furthermore, an acid-responsive ketal hydrolysis, accompanied by cleavage of the biocompatible small molecules, acetone and benzyl alcohol, could be confirmed too. Encouraged by these results, amphiphilic block copolymers were synthesized using an $mPEG_{113}$-OH macroinitiator. These block copolymers were tested for their ability to self-assemble into monomodal spherical polymeric micelles. A detailed acid degradation study of these nanoparticles revealed a proton-catalyzed micelle unfolding within suitable timeframes for drug-administration applications. In addition, the encapsulation and pH-responsive release of active cargoes was successfully achieved. By monitoring the UV absorbance of Nile red, the cargo release was exclusively achieved upon polymeric micelle degradation in both acidic and basic environments, while the drug loading and micelle integrity remained stable under physiological conditions. The internalization of dye-loaded polymeric micelles by macrophages was demonstrated by fluorescence microscopy and flow cytometry. During multi-angle DLS studies in human blood plasma, no aggregation was observed for the drug-loaded particles indicating the absence of unfavorable protein absorption. Finally, the cellular delivery of the TLR7/8 agonist CL075 into macrophages was confirmed. Pronounced immune stimulatory receptor activation of macrophages was only observed for the drug-loaded particles, in analogy to the free drug. Taking these properties into account together with the high biocompatibility and biodegradability of the polycarbonate carrier scaffold, the introduced polymeric micelles can be considered as a highly promising delivery system for multi-pH-responsive release applications.

Data availability

The data supporting this article have been included as part of the ESI PDF document.†

Conflicts of interest

There are no conflicts to declare.

Acknowledgements

The authors thank Hans-Joachim Räder, Jutta Schnee and Stephan Türk for MALDI-TOF MS measurements, Stefan Spang and Manfred Wagner for NMR measurements, and Christine Rosenauer for multi-angle DLS measurements (all at Max Planck Institute for Polymer Research, Mainz). The authors kindly acknowledge funding by the DFG through the Emmy Noether program (project number 417278389, to L. N.) as well as the SFB 1066 (project number 213555243, to P. B. and L. N.). They are also grateful for financial support by the European Research Council (ERC) under the European Union's Horizon 2020 research and innovation program (ERC CoG SUPRAVACC 819856, to P. B.). J. E. was financially supported by the Studienstiftung des deutschen Volkes.

References

1 M. A. Postow, R. Sidlow and M. D. Hellmann, *N. Engl. J. Med.*, 2018, **378**, 158–168.
2 D. J. Irvine and E. L. Dane, *Nat. Rev. Immunol.*, 2020, **20**, 321–334.
3 R. Ferrari, M. Sponchioni, M. Morbidelli and D. Moscatelli, *Nanoscale*, 2018, **10**, 22701–22719.
4 A. Kumari, S. K. Yadav and S. C. Yadav, *Colloids Surf., B*, 2010, **75**, 1–18.
5 Z. Yu, X. Shen, H. Yu, H. Tu, C. Chittasupho and Y. Zhao, *Pharmaceutics*, 2023, **15**, 775–803.
6 M. Talelli, M. Barz, C. J. F. Rijcken, F. Kiessling, W. E. Hennink and T. Lammers, *Nano Today*, 2015, **10**, 93–117.
7 S. Endres, E. Karaev, S. Hanio, J. Schlauersbach, C. Kraft, T. Rasmussen, R. Luxenhofer, B. Böttcher, L. Meinel and A. C. Pöppler, *J. Colloid Interface Sci.*, 2022, **606**, 1179–1192.
8 A. Pöppler, M. M. Lübtow, J. Schlauersbach, J. Wiest, L. Meinel and R. Luxenhofer, *Angew. Chem.*, 2019, **131**, 18712–18718.
9 A. Birke, J. Ling and M. Barz, *Prog. Polym. Sci.*, 2018, **81**, 163–208.
10 H. Kim, T. Uto, T. Akagi, M. Baba and M. Akashi, *Adv. Funct. Mater.*, 2010, **20**, 3925–3931.
11 N. Bhattarai, S. R. Bhattarai, M. S. Khil, D. R. Lee and H. Y. Kim, *Eur. Polym. J.*, 2003, **39**, 1603–1608.
12 C. Czysch, C. Medina-Montano, Z. Zhong, A. Fuchs, J. Stickdorn, P. Winterwerber, S. Schmitt, K. Deswarte, M. Raabe, M. Scherger, F. Combes, J. De Vrieze, S. Kasmi, N. N. Sandners, S. Lienenklaus, K. Koynov, H. J. Räder, B. N. Lambrecht, S. A. David, M. Bros, H. Schild, S. Grabbe, B. G. De Geest and L. Nuhn, *Adv. Funct. Mater.*, 2022, **32**, 2203490.
13 R. Gref, M. Lück, P. Quellec, M. Marchand, E. Dellacherie, S. Harnisch, T. Blunk and R. H. Müller, *Colloids Surf., B*, 2000, **18**, 301–313.
14 A. Abuchowski, J. R. McCoy, N. C. Palczuk, T. van Es and F. F. Davis, *J. Biol. Chem.*, 1977, **252**, 3582–3586.
15 Y. Nagasaki, T. Okada, C. Scholz, M. Iijima, M. Kato and K. Kataoka, *Macromolecules*, 1998, **31**, 1473–1479.
16 C. Czysch, T. Dinh, Y. Fröder, L. Bixenmann, P. Komforth, A. Balint, H.-J. Räder, S. Naumann and L. Nuhn, *ACS Polym. Au*, 2022, **2**, 371–379.

17 C. Czysch, C. Medina-Montano, N. J. K. Dal, T. Dinh, Y. Fröder, P. Winterwerber, K. Maxeiner, H. J. Räder, D. Schuppan, H. Schild, M. Bros, B. Biersack, F. Feranoli, S. Grabbe and L. Nuhn, *Macromol. Rapid Commun.*, 2022, **43**, 2200095.
18 Y. Matsumura and H. Maeda, *Cancer Res.*, 1986, **46**, 6387–6392.
19 B. Ghosh and S. Biswas, *J. Controlled Release*, 2021, **332**, 127–147.
20 W. Islam, T. Niidome and T. Sawa, *J. Pers. Med.*, 2022, **12**, 1964–1983.
21 Y. Barenholz, *J. Controlled Release*, 2012, **160**, 117–134.
22 J. A. Silverman and S. R. Deitcher, *Cancer Chemother. Pharmacol.*, 2013, **71**, 555–564.
23 D. Hwang, J. D. Ramsey and A. V. Kabanov, *Adv. Drug Delivery Rev.*, 2020, **156**, 80–118.
24 R. G. Thomas, S. P. Surendran and Y. Y. Jeong, *Front. Mol. Biosci.*, 2020, **7**, 610533.
25 M. Kanamala, W. R. Wilson, M. Yang, B. D. Palmer and Z. Wu, *Biomaterials*, 2016, **85**, 152–167.
26 W. Gao, J. M. Chan and O. C. Farokhzad, *Mol. Pharmaceutics*, 2010, **7**, 1913–1920.
27 A. Van Driessche, A. Kocere, H. Everaert, L. Nuhn, S. Van Herck, G. Griffiths, F. Fenaroli and B. G. De Geest, *Chem. Mater.*, 2018, **30**, 8587–8596.
28 Z. Liu and N. Zhang, *Curr. Pharm. Des.*, 2012, **18**, 3442–3451.
29 C. Wang, G. Wang, Z. Wang and X. Zhang, *Chem. – Eur. J.*, 2011, **17**, 3322–3325.
30 N. Murthy, Y. X. Thng, S. Schuck, M. C. Xu and J. M. J. Fréchet, *J. Am. Chem. Soc.*, 2002, **124**, 12398–12399.
31 L. Nuhn, N. Vanparijs, A. De Beuckelaer, L. Lybaert, G. Verstraete, K. Deswarte, S. Lienenklaus, N. M. Shukla, A. C. D. Salyer, B. N. Lambrecht, J. Grooten, S. A. David, S. De Koker and B. G. De Geest, *Proc. Natl. Acad. Sci. U. S. A.*, 2016, **113**, 8098–8103.
32 J. Stickdorn, L. Stein, D. Arnold-Schild, J. Hahlbrock, C. Medina-Montano, J. Bartneck, T. Zieß, E. Montermann, C. Kappel, D. Hobernik, M. Haist, H. Yurugi, M. Raabe, A. Best, K. Rajalingam, M. P. Radsak, S. A. David, K. Koynov, M. Bros, S. Grabbe, H. Schild and L. Nuhn, *ACS Nano*, 2022, **16**, 4426–4443.
33 L. Nuhn, S. Van Herck, A. Best, K. Deswarte, M. Kokkinopoulou, I. Lieberwirth, K. Koynov, B. N. Lambrecht and B. G. De Geest, *Angew. Chem., Int. Ed.*, 2018, **57**, 10760–10764.
34 S. Van Herck, K. Deswarte, L. Nuhn, Z. Zhong, J. P. Portela Catani, Y. Li, N. N. Sanders, S. Lienenklaus, S. De Koker, B. N. Lambrecht, S. A. David and B. G. De Geest, *J. Am. Chem. Soc.*, 2018, **140**, 14300–14307.
35 S. Van Herck and B. G. De Geest, *Sci. China: Chem.*, 2020, **63**, 504–512.
36 B. Liu and S. Thayumanavan, *J. Am. Chem. Soc.*, 2017, **139**, 2306–2317.
37 D. Chen and H. Wang, *J. Nanosci. Nanotechnol.*, 2014, **14**, 983–989.
38 Y. Shi, M. J. Van Steenbergen, E. A. Teunissen, L. Novo, S. Gradmann, M. Baldus, C. F. Van Nostrum and W. E. Hennink, *Biomacromolecules*, 2013, **14**, 1826–1837.
39 Y. Shi, R. Van Der Meel, B. Theek, E. Oude Blenke, E. H. E. Pieters, M. H. A. M. Fens, J. Ehling, R. M. Schiffelers, G. Storm, C. F. Van Nostrum, T. Lammers and W. E. Hennink, *ACS Nano*, 2015, **9**, 3740–3752.
40 J. P. Guthrie, *Can. J. Chem.*, 1977, **55**, 3562–3574.
41 N. Hamon, C. C. Mouline and M. Travert, *Eur. J. Org. Chem.*, 2017, **2017**, 4803–4819.
42 T. F. Al-Azemi and K. S. Bisht, *Macromolecules*, 1999, **32**, 6536–6540.
43 T. F. Al-Azemi and K. S. Bisht, *J. Polym. Sci., Part A: Polym. Chem.*, 2002, **40**, 1267–1274.
44 F. Nederberg, B. G. G. Lohmeijer, F. Leibfarth, R. C. Pratt, J. Choi, A. P. Dove, R. M. Waymouth and J. L. Hedrick, *Biomacromolecules*, 2007, **8**, 153–160.
45 E. W. P. Tan, J. L. Hedrick, P. L. Arrechea, T. Erdmann, V. Kiyek, S. Lottier, Y. Y. Yang and N. H. Park, *Macromolecules*, 2021, **54**, 1767–1774.
46 M. Bagheri, J. Bresseleers, A. Varela-Moreira, O. Sandre, S. A. Meeuwissen, R. M. Schiffelers, J. M. Metselaar, C. F. Van Nostrum, J. C. M. Van Hest and W. E. Hennink, *Langmuir*, 2018, **34**, 15495–15506.
47 S. H. Bhagchandani, F. Vohidov, L. E. Milling, E. Y. Tong, C. M. Brown, M. L. Ramseier, B. Liu, T. B. Fessenden, H. V. T. Nguyen, G. R. Kiel, L. Won, R. S. Langer, S. Spranger, A. K. Shalek, D. J. Irvine and J. A. Johnson, *Sci. Adv.*, 2023, **9**, 1–19.
48 M. G. Carstens, C. F. van Nostrum, R. Verrijk, L. G. J. Leede, D. J. A. Crommelin and W. E. Hennink, *Pharm. Nanotechnol.*, 2007, **97**, 506–518.
49 S. J. De Jong, E. R. Arias, D. T. S. Rijkers, C. F. Van Nostrum, J. J. Kettenes-Van Den Bosch and W. E. Hennink, *Polymer*, 2001, **42**, 2795–2802.
50 E. R. Gillies, T. B. Jonsson and J. M. J. Fréchet, *J. Am. Chem. Soc.*, 2004, **126**, 11936–11943.
51 L. Bixenmann, J. Stickdorn and L. Nuhn, *Polym. Chem.*, 2020, **11**, 2441–2456.
52 K. Fukushima, *Biomater. Sci.*, 2016, **4**, 9–24.
53 Z. Zhang, R. Kuijer, S. K. Bulstra, D. W. Grijpma and J. Feijen, *Biomaterials*, 2006, **27**, 1741–1748.
54 K. Rausch, A. Reuter, K. Fischer and M. Schmidt, *Biomacromolecules*, 2010, **11**, 2836–2839.

